Research Article | Vol. 31, No. 17 / 14 Aug 2023 / Optics Express 28423
Optics EXPRESS

Opto-microfluidic coupling between optical waveguides and tilted microchannels in lithium niobate

RICCARDO ZAMBONI,[1,2,*] LUDOVIC GAUTHIER-MANUEL,[3] ANNAMARIA ZALTRON,[2] LIANA LUCCHETTI,[4] MATHIEU CHAUVET,[3] AND CINZIA SADA[2]

[1]*Institute of Applied Physics, University of Münster (WWU), Correnstr. 2/4, Münster 48149, Germany*
[2]*Dipartimento di Fisica e Astronomia G. Galilei, Universitá di Padova, 35131 Padova, Italy*
[3]*FEMTO-ST Institute, UMR 6174, University of Franche-Comté, 15B Avenue des Montboucons, 25000 Besançon, France*
[4]*Dipartimento Scienze e Ingegneria dei Materiali e dell'Ambiente e Urbanistica, Universitá Politecnica delle Marche, 60131 Ancona, Italy*
[*]*riccardo.zamboni@uni-muenster.de*

Abstract: This work presents a reconfigurable opto-microfluidic coupling between optical waveguides and tilted microfluidic channels in monolithic lithium niobate crystal. The light path connecting two waveguide arrays located on opposite sides of a microfluidic channel depends on the refractive index between the liquid phase and the hosting crystal. As a result, the optical properties of the flowing fluid, which is pumped into the microfluidic channel on demand, can be exploited to control the light pathways inside the optofluidic device. Proof-of-concept applications are herein presented, including microfluidic optical waveguide switching, optical refractive index sensing, and wavelength demultiplexing.

1. Introduction

Since Jones coined the term "optofluidics" in 1985 [1], the combination of microfluidic and optical components has been a major breakthrough for several applications [2,3]. The interaction of these two technologies provides unprecedented flexibility for optical devices due to the optical properties of fluids [4–7], and an optical toolkit [8–10] for microfluidic chips. One of the most widely used methods for integrating microfluidics and optics is using optical fibers in microfluidic devices [11]. Optical fibers can either illuminate from the top or aside, i.e., through the microfluidic channel. On the one hand, this configuration enables tunable optical elements [12] or light shaping [13,14] using microfluidic systems. On the other hand, a local light source provided efficient optical sensing within the microfluidic devices [15], e.g., for biochemical analysis [16], for Raman spectroscopy [17], for dynamic properties [18] of liquids, or for lasing [19,20]. Moreover, the use of optical forces for manipulation purposes was made possible by the use of optical fibers in microfluidics [21–23].

However, the critical alignment of the optical fibers does not guarantee a sufficient level of reproducibility for mass production. In addition, the design of devices with such parallelized probe arrays is limited by the bulkiness of the fibers and integration issues. The replacement of optical fibers with monolithic optical waveguides represents a promising solution to achieve miniaturized and fully integrated systems. Over the past two decades, several efforts have been made to combine optical waveguides with a microfluidic channel in the same substrate, either by laser writing [24] or lithographic techniques [25]. The most significant improvements are

#495406 https://doi.org/10.1364/OE.495406
Journal © 2023 Received 16 May 2023; revised 5 Jul 2023; accepted 5 Jul 2023; published 10 Aug 2023

Optics EXPRESS

undoubtedly the precise alignment between optical and microfluidic structures and the realization of complex optical systems [26,27]. Several materials have proven to be optimal substrates for hosting both microfluidic channels and optical waveguides, ranging from polymers such as PDMS [28] or SU8 [29] to common optic materials such as glass [24,25] or lithium niobate [30,31]. The latter is a well-known material in optics for its outstanding optical properties [32], making it a workhorse for several applications [33], such as holography [34], frequency doubling [35,36], and miniaturized optical components [37,38] to name a few. Recently, this material has found notable success in the microfluidic field, e.g., for droplet [39–42], biosample [43–45], and particle [46,47] manipulation within channel geometries with typical sizes of micrometers. In addition, the introduction of the microfluidic stages has increased opportunities for optical applications, such as microlenses [48,49], or in combination with liquid crystals [50–52]. The high performance of the miniaturized components realized in lithium niobate has opened up new possibilities in optical sensing, e.g., droplet counting and velocimetry [27,31,53], spectral measurement [54,55], novel applications in combination with soliton waveguides [30,56].

The full benefits of combining miniaturized optical components in lithium niobate with the optical flexibility of fluids in microfluidic systems have yet to be reaped. This work represents a further step in this direction, presenting a microfluidic-based manipulation stage that controls the light path between optical waveguides realized in lithium niobate. The opto-microfluidic system consists of an array of parallel optical waveguides interacting with a tilted microfluidic channel (see Fig. 1(a)). Such a dense array cannot be realized in a compact way by a bundle of fibers due to its bulkiness. The chips used in this work contain more than 500 waveguides (divided into different arrays) and are pocket-sized (see Fig. 1(b)). Inside the microfluidic channel, the optical path of light coming from the waveguides depends on the optical properties of the medium inside the channel. In particular, the microfluidic channel shifts the incoming light due to the refraction

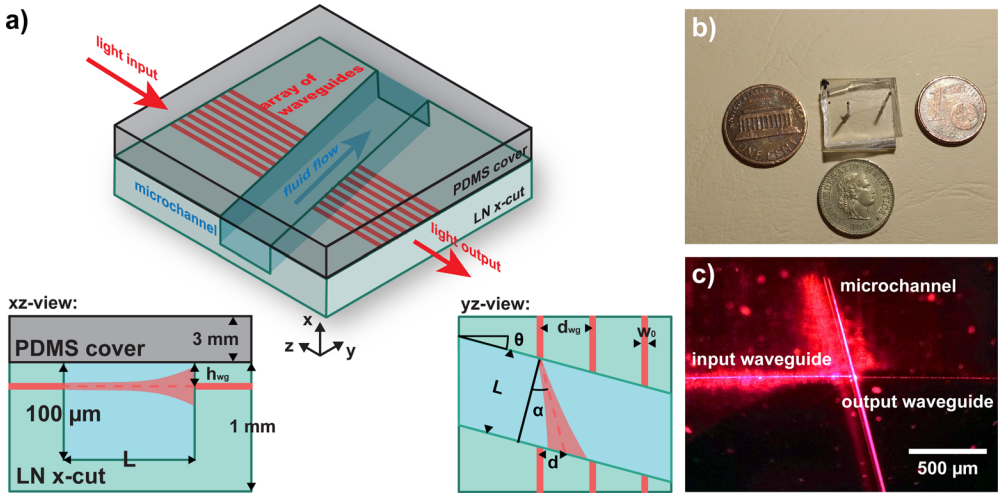

Fig. 1. (a) Schematic of the device: the lithium niobate substrate, the waveguide array crossed by the tilted channel, and the PDMS cover. The 2D xz-view shows the thickness of the different layers and the location of the channel and waveguides. The 2D yz-view highlights the main parameters for the opto-microfluidic coupling: the shift d between the input and output waveguide, the angles α, θ, and the width of the channel L. (b) Image of a device with a dimension of 17x17 mm^2, with 20 different waveguide arrays containing each about 50 waveguides. (c) Top view with a microscope of the channel coupling the light from the input waveguide to a shifted output waveguide. The red line is the evanescent loss of light from the waveguide.

Optics EXPRESS

with injected fluid, allowing complete control of the light propagation with the microfluidics. Then, one of the output waveguides on the other side of the channel collects the incoming light. As a proof of concept, the proposed configuration is used to switch the light coupling between waveguides by the injection of different fluids inside the channel. Similarly, the system is also shown to behave as a refractive index sensor or an optical demultiplexer for separating spectral components.

2. Working principle

The opto-microfluidic configuration uses the refraction of the incoming light from the waveguides with the fluids inside the microfluidic channel. Due to refractive index change on the interface of the channel walls, the light is refracted by the first encountered channel wall. As long as the incident angle is smaller than the critical angle, the beam propagates from the waveguide inside the channel. Another refraction occurs when the light reaches the second channel interface, and it can couple inside a waveguide located on the other side with respect to the illuminating ones. The beam path between the two channel walls is shifted by a distance d as shown in Fig. 1(a). If the two arrays are aligned and d is a multiple of the distance between the waveguides d_{wg}, then the light is transferred to $N = d/d_{wg}$ waveguides of the array next to the input waveguide. The value d can be predicted by simple consideration of ray optics as:

$$d(L, n_{LN}, n_F, \theta) = \frac{sin(sin^{-1}(\frac{n_{LN}}{n_F}(\lambda)sin\theta) - \theta)L}{cos(sin^{-1}(\frac{n_{LN}}{n_F}(\lambda)sin\theta))} \tag{1}$$

where θ is the tilt angle between the microfluidic channel and the waveguides, L is the channel width, $n_{LN}(\lambda)$ and $n_F(\lambda)$ are the refractive indices of the lithium niobate and the fluid depending on the wavelength λ of the light, respectively (see Fig. 1(a)). The refractive index of the lithium niobate is the ordinary one since the waveguides are propagating along the polar axis (see the crystal orientation in Fig. 1(a)). It is worth mentioning that the tilt angle θ is equal to the incidence angle of the first refraction.

3. Experimental

The microfluidic channels and the optical waveguides are realized on the same monolithic lithium niobate platform. The procedure used for the realization of the final device is presented in the following. Then, the experimental setup used for the characterization of the opto-microfluidic coupling is described.

3.1. Fabrication

The optical waveguides are Ti-indiffused into 3-inch commercial x-cut $LiNbO_3$ wafers (LN, thickness: 1 mm, by Crystal Technology Inc., Palo Alto, CA, USA), resulting in single-mode waveguides in the visible range. The process consists of three main steps (see first three sketches in Fig. 2(a)). First, a lithography technique produces a homogeneous coating of photoresist S1805 (Dow Chemical, Midland, MI, USA) in the region where the Titanium will not be diffused. Then, a thin and homogeneous layer of titanium is deposited via magnetron sputtering. Titanium stripes of 5.2 ± 0.3 µm width and 41 ± 5 nm thickness are, then, obtained by lift-off, removing completely the resist and the excess of titanium. The diffusion inside the crystal is performed by thermal treatment inside a tubular furnace (F-VS 100-500/13 Carbolite Gero, Neuhausen, Germany) at $1030°C$ for two hours in O_2 atmosphere. Secondary ions mass spectrometry and Rutherford backscattering spectrometry reveal that the dopant concentration follows an in-depth semi-Gaussian profile with a mean diffused depth $h_{wg} = 1.13 \pm 0.05$ µm and maximum titanium concentration at the surface of $(1.06 \pm 0.04) \cdot 10^{21}$ cm^{-1}. The refractive indices variations induced by Titanium doping [57] are $\Delta n_e = (1.12 \pm 0.03) \cdot 10^{-2}$ and $\Delta n_o = (0.66 \pm 0.03) \cdot 10^{-2}$ for

Optics EXPRESS

extraordinary and ordinary indices, respectively. A detailed description of the lithographic process with all parameters and the titanium profile analysis are given in [54]. The final waveguides are z-propagating and single-mode with Gaussian profiles in both transverse directions with an average diameter along the y-axis of $w_0 = 3.6 \pm 0.3$ µm (see section 2 in Supplement 1), and propagation loss of 4 ± 2 dB cm^{-1} at 632.9 nm measured by a cut-back technique.

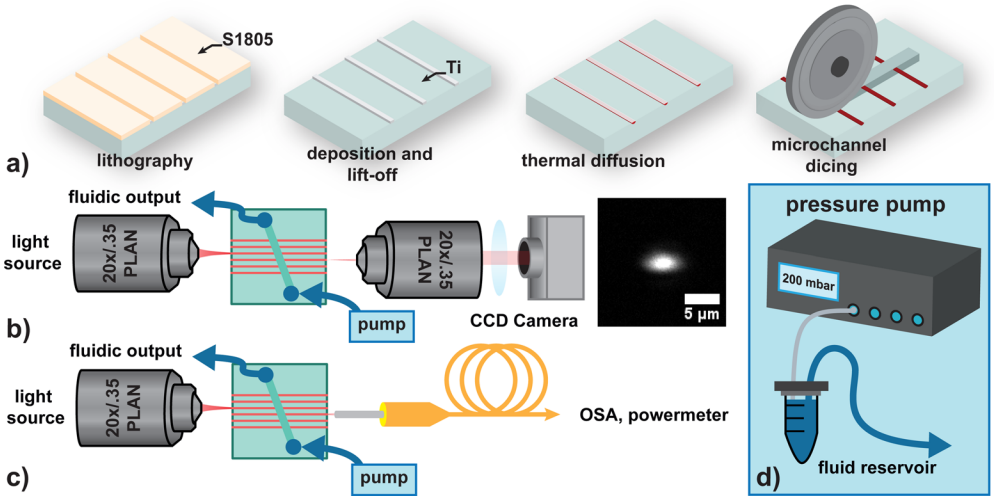

Fig. 2. (a) Sketches showing the fabrication process of the optofluidic device. The light from the input waveguide is either collected by an optical fiber (b) or a microscope objective (c). The near field of the output beam is imaged by a CCD camera with a tube lens. Coupling with fiber is not reported here because it is similar to the example shown for the light collection. (d) In each experiment, the fluids are injected with a pressure pump. The entire figure is not in scale to better highlight each part.

These single-mode waveguides are arranged in arrays characterized by d_{wg}, the distance between centers of consecutive waveguides. Every single sample has arrays of more than 50 waveguides with $d_{wg} = [10, 11, 12, 13, 14, 15, 20, 25]$ µm. Due to the thermal diffusion, the width of the waveguides is larger than the nominal width of the stripe. The analysis of the distance between consecutive stripes showed an average mismatch of $6 \pm 3\%$. This value is the result of the measurement of the waveguide arrays by optical microscopy, more details are provided in section 3 of Supplement 1. Twenty-four samples of 17x17 cm^2 were obtained from two LN wafers. The samples are diced with a precision saw (DISCO DAD 3350) at 10000 rpm and linear velocity of 0.2 mm s^{-1} equipped with a polishing blade. The same dicing technique is used to engrave the fluidic channel (Fig. 2(a)). Two kinds of channels were engraved with a width L of 50 and 200 µm and the same depth of 100 µm. Notably, the channels were engraved after the diffusion of the waveguide, thus the input and output arrays are self-aligned. Fluidic channels with different tilted angles $\theta = [10, 12.5, 13.3, 14.1, 15.5, 20, 21.5, 25, 27, 28, 30, 31]°$ with respect to the y-axis were fabricated. Finally, the channels were sealed using a polydimethylsiloxane (PDMS, Dow Chemical) substrate. Inlet and outlet tubings were embedded in the PDMS cover to connect the device and the pump. A covalent bonding between the PDMS and the crystal is obtained by plasma activation of both substrates for 1 min at 600 W with a continuous O_2 flow of 10 cm^3 min^{-1} at a pressure of $3 \cdot 10^{-3}$ mbar. The microfluidic performances of each channel have been established even for a multi-phase system as in [58].

Optics EXPRESS

3.2. Opto-microfluidic setup

The experimental setup consists of two main parts: the optical one for light coupling and detection (see Fig. 2(b) and Fig. 2(c)), and the microfluidic one for fluid injection (see Fig. 2(d)). The fluids are injected at a constant pressure of 200 mbar by a pressure pump (OB1 MK3+, Elveflow). Distilled water is used to test the system, and 8 aqueous solutions of $CaCl_2$ are tested for refractive index sensing. The value of $CaCl_2$ concentration, C_{CaCl_2}, and the respective refractive index of the solutions are listed in Table 1.

Table 1. Solutions are made by solving the $CaCl_2$ in water.[a]

C_{CaCl_2} (%)	0	2	5	10	14	20	26	30
n_F	1.332	1.3378	1.3451	1.3575	1.3677	1.3839	1.4008	1.4121

[a]The refractive indices at a wavelength of 632.8 nm are obtained by a linear relationship starting from the refractive index of water and the value of the concentrations [59].

Three light sources are used in this work: a He-Ne laser (maximum power 1 mW and $\lambda = 632.8$ nm) for the refractive index sensing, a CW diode laser (maximum power 8 mW and $\lambda = 655$ nm) for the optical switching and characterization measurements, and a broadband source based on a supercontinuum fiber (more details are given in section 4 of Supplement 1). In each case, the input power is an order of magnitude lower than the one causing optical damage. The photorefractive properties of the material, therefore, have no effect on the performance of the device. The light beam is coupled with the waveguides in a butt-coupling configuration using a Plan Achromat Objective 20x/0.35 except for the broadband source, which is fiber coupled. In the first case, the diameter of the focused beam has a minimum value of 5.1 ± 0.9 µm, which ensures the excitation of a single waveguide at once. To collect near-field images of the output waveguides (see Fig. 2(b)), a similar microscope objective is used in combination with a charge-coupled device (CCD, LaserCam-HR II, Coherent). For spectral or power measurement, an optical fiber with an inner diameter of 7.2 ± 0.7 µm is precisely aligned by a 3D nano-positioning stage (see Fig. 2(c)), and it is connected to either an Optical Spectrum Analyzer (AQ6373B, Yokogawa) or a photodiode (S120C, Thorlabs). In every case except for the broadband source, the polarization of the incoming light is opportunely polarized to excite TE mode.

4. Results and discussion

The results in this paper are based on Eq. (1) and are completely available in Dataset 1 [67]. Equation (1) describes the refraction of the light beam at the interfaces. Thus, a preliminary discussion on the quality of the channel walls is mandatory and detailed in section 2 of Supplement 1.

4.1. Transmission at the interfaces between channel and waveguides

The technique used to engrave the channel is similar to the one to realize for the ridge waveguides [60] and it is meant to obtain optical quality surfaces. A complete characterization of the surface roughness with an atomic force microscope and scanning electron microscope is given in [58]. We observed that the light transmission due to the presence of a 200 µm wide straight channel ($\theta = 0°$) filled with air decreases to only 38% of its initial value, and it can be increased by injecting fluids. The power at the input for this measurement was 0.5 mW, thus allowing low-power applications. Also, waveguides in lithium niobate have been reported to sustain high power transmission [60]. A narrower channel offers higher transmission, due to the lower dispersion of the beam inside the channel. However, the qualitative inspection of tilted channels in Fig. 3 reveals the presence of scratches on the upper edge of the 50 µm wide channel. The comparison between Fig. 3(a) and 3b shows a higher density of scratches for the channel made with a 50 µm thick blade with

Optics EXPRESS

respect to the one made with a 200 µm thick one. The measurement with a profilometer P-10 (KLA Tencor, California, USA) of the channel width L gives 201 ± 1 and 61 ± 2 µm (average over more than 10 profiles for each channel and different channel), respectively. The scratches and the higher mismatch from the nominal blade width suggest the occurrence of blade oscillations during the dicing for the 50 µm thick blade, which is less stable due to its thinness. This behavior might be improved by adjusting the dicing machine parameters. A systematic investigation has been performed on the best procedure to get sharp and scratched-free microfluidic channels. The best performance is achieved with a channel engraved at a positive angle with respect to the y-axis of the crystal, in agreement with the crystalline structure of the material (see section 2 of Supplement 1). In this configuration, the transmission is similar to the straight channel configuration for both channel widths.

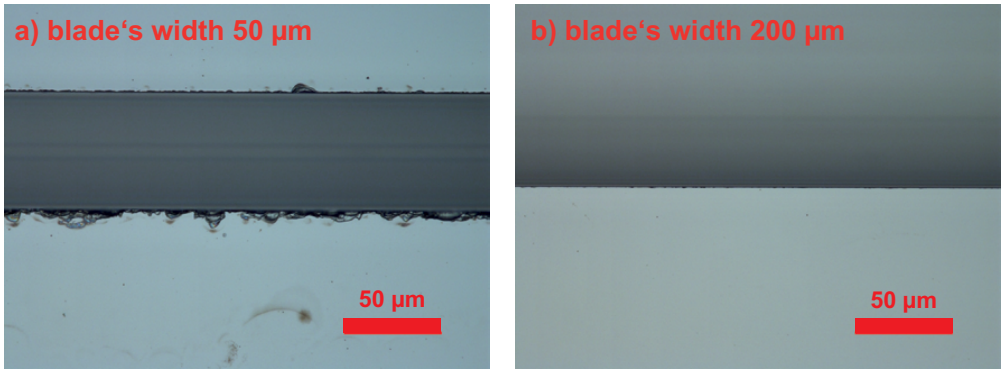

Fig. 3. Microscope images with 50x/0.6 Plan Objective (Nikon) of channels with a tilt angle of 30° and with two different widths: (a) realized with a 50 µm thick blade, (b) with one 200 µm thick, respectively. In (b), only one side of the channel is shown to better compare the quality of the edge with the worst side of the channel in (a) at the same magnification.

4.2. *Proof of the working principle and optical switching*

According to Eq. (1), fluids with a lower refractive index n_F shift the light to a longer distance d. Thus, the optical path of the light within the channel is longer. When the distance d is equal to d_{wg} with the proper media inside the channel, light can switch to a lateral output waveguide (see Fig. 4(a)). To demonstrate this optical switching, different arrays (i.e., with different d_{wg}) and channels (i.e., with different θ) are tested sequentially by injecting air and water. Figure 4(b) shows an example of the switch for a channel with $\theta = 13.3°$, a light source $\lambda = 655$ nm and an array with $d_{wg} = 11$ µm. Only one waveguide of the output array transmits light, and its position depends on the refractive index of the medium inside the channel. If air flows through the channel, the refraction angle is greater than in water according to Eq. (1), and consequently, this difference results in two excited different output waveguides. Measuring the shift d between the input and output waveguides requires a reference for the position of the input waveguides. To this aim, each sample has a reference waveguide, which is not intercepted by the channel (see Fig. 4(a)). The reference waveguide has a known distance from all other waveguides, allowing alignment to the input waveguide and setting the origin of d to that waveguide. The distance d is measured as the separation between the centroids of the Gaussian profiles along the y-axis. Figure 4(c) shows an example of these profiles corresponding to the output of Fig. 4(b). The three centroids (vertical dashed lines) of the Gaussian fits (black lines) correspond to $d = 10.5$ µm and 21.3 µm, which agrees with the measured distance between the waveguides for the array $d_{wg} = 11$ µm (considering the adjustment to the nominal d_{wg} due to thermal diffusion). The

Optics EXPRESS

graph in Fig. 4(d) shows the measured d compared with Eq. (1) prediction for different arrays and angles θ for both water and air. The values of d are normalized by the width of the channel L to compare data obtained with different channel widths. The normalized d_{wg} results agree with the values predicted by Eq. (1) (solid lines). For θ>26°, we observed no transmission in any of the waveguides of the array, since the angle of incidence is larger than the critical angle $\theta_c(n_F)$. Similarly, no light is collected if d does not match a multiple of d_{wg}, or the beam size does not overlap with any output waveguides. Therefore, the parameters for an efficient switching behavior have to be chosen to have $\theta<\theta_c(n_F)$ and to achieve $d(n_F, \theta) = d_{wg}$. During the propagation inside the channel, the beam diameter increases due to diffraction, and consequently, the beam extension across the channel is larger than the initial mode size. The diffraction has been taken into account considering a Gaussian beam propagation along the optical path (more details are given in section 5 of Supplement 1), and the beam diameter after crossing the channel is highlighted by the two dashed lines in Fig. 4(d). Only the diffraction along the length of the microchannel (y-axis in Fig. 1(a)) matters for the considerations. The diffraction along the vertical direction (x-axis in Fig. 1(a)) causes losses but does not change the working principle of the proposed device. Furthermore, along this direction the waveguide mode has an initial width that is at least twice w_0, thus making negligible losses compared to diffraction in the other direction. Notably, the beam diffraction inside the channel is insufficient to excite more than one waveguide in this range of angle θ. This feature allows the system to switch precisely between two waveguides by the microfluidic control. The switching process is only limited by the angle of incidence, which has to be lower than the critical angle (26° for lithium niobate and air). Nevertheless, this feature can be also exploited for blocking the beam and switching between transmission and total reflection configurations. The switching operation speed depends on the performance of the microfluidic actuator, which injects new fluid and switches between two fluids. There are several publications about actuators that can be directly integrated and can be easily controlled electronically [61]. Moreover, other microfluidic features can be implemented to increase the performance of this switch, such as the use of droplets [31,62] to introduce complex configuration.

4.3. Refractive index sensing

The output signal described in the previous section depends strongly on the refractive index of the medium in the channel n_F. The latter is univocally related to the output waveguide of the array and, thus, the system works as an optical sensor for the refractive index of the fluid flowing inside the channel. To enhance the difference in a shift among different n_F, larger θ compared to the previous application have been used. The performances are tested with the 8 aqueous solutions listed in Table 1 inside a channel with θ = 29°. Each fluid is injected consecutively increasing the refractive index. Simultaneously, the waveguide output is captured in an array of d_{wg} = 10 µm, with the analysis of the profile as described in Fig. 4. For such large θ, the diffraction makes the size of the beam larger than the d_{wg} = 10 µm, and multiple output waveguides are excited by light propagating through the channel. The example in Fig. 5(a) shows this effect in the near-field images of the output for three different solutions. It is worth mentioning that the three images are not aligned along the x-axis. The equivalent realigned profiles with respect to the reference are shown in Fig. 5(b). The overall intensity of the entire set of excited waveguides follows a Gaussian shape, which is related to the beam size propagated through the channel. The value of d is, therefore, measured as the centroid of the Gaussian interpolation of the intensities transmitted by each waveguide of the array. The measured values of d by this analysis are compared with Eq. (1) in Fig. 5(c). The results (listed in Supplement 1) follow again the prediction given by Eq. (1). Therefore, the output waveguides provide an instantaneous measurement of the refractive index of the liquid flowing in the channel n_F. The partial derivative of Eq. (1) with respect to n_F provides also a definition of the sensitivity S of the proposed method (see section 6 of Supplement 1). In Fig. 5(d), S is plotted in a wider range of refractive indices for different channel

Optics EXPRESS

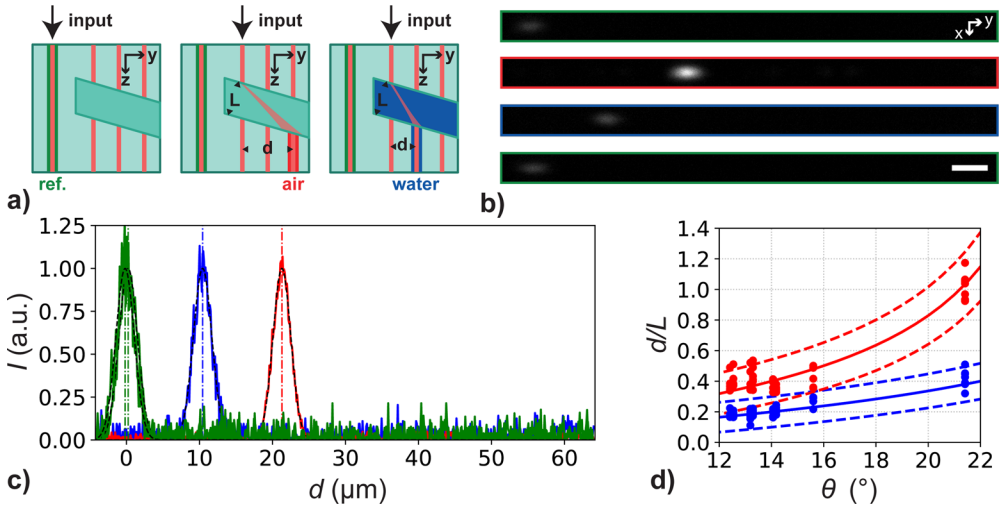

Fig. 4. (a) Sketch of the optical switching operations. First, the input is the reference waveguide, then, the input is the first waveguide of the array and the output is collected with air in the channel. After the injection of water, the switch occurs to a closer waveguide to the input one. Finally, the reference is observed again. (b) Near-field images of the output waveguide for a switching operation for a system with $\theta = 13.3°$, $\lambda = 655$ nm, and the $d_{wg} = 11$ μm: first reference (green), for the channel filled with air (red), with water (blue) and reference again (green). Every image is captured with an optical density filter to avoid saturation of the camera: $OD = 5.3$ for air and $OD = 7$ for the others.

parameters. For a channel like the one used for the data in Fig. 5(c) ($\theta = 29°$ and $L = 200$ μm), S is equal to 206 μm RIU^{-1} for $n_F = 1.3$. In practice, the sensitivity depends also on the value of d_{wg}, which has a practical limit given by the w_0. For $d_{wg} = 10$ μm, this result corresponds to a minimum variation $\Delta n_F = (d_{wg} - w_0)/S = 0.02$ RIU (considering the actual experimental value $d_{wg} = 8.7$ μm and also the width of the waveguides) to switch completely between two consecutive waveguides. However, the experimental analysis is based on multiple waveguides signal, which allows for enhanced effective sensitivity. In detail, two patterns like the ones reported in Fig. 5(b) can be distinguished even as long as the intensity pattern among multiple waveguides changes. If there is an intensity change in the light pattern measure measured by multiple waveguides sufficient to distinguish the Gaussian functions related to two different indices of refraction, the system is able to distinguish the signal. A decrease of d_{wg} leads to an enhanced sensitivity for two reasons: the minimum Δn_F decreases and the number of waveguides collecting signals can increase. Experimentally, we observed an uncertainty of 1 μm on the determination of the centroid, and thus the minimum distance between two centroids should be at least three times this value corresponding to $\Delta n_F = 3 \times 1\mu m/S = 0.015$ RIU. Since the sensitivity of the final device depends on the fabrication parameters, the device can be optimized to enhance sensitivities. For instance, S is inversely proportional to L and lower d_{wg} enhanced the sensitivity. Therefore, $L = 1000$ μm and $d_{wg} = 5$ μm allows to achieve $\Delta n_F = 5\mu m/S(1000\mu m) = 0.005$ RIU. It is worth noting that this value of S is about 10 times larger than the conventional commercial Abbe refractometers. However, Abbe refractometers are bulky instruments, are not portable, and cannot be embedded in the microfluidic circuit. This method provides a real-time measurement in pocket size device on flowing liquid, which can be further used in microfluidic operation without any waste. Sensitivity can also be improved by collecting the light after multiple reflections within the channel, which we expect to be detectable with greater power input.

Optics EXPRESS

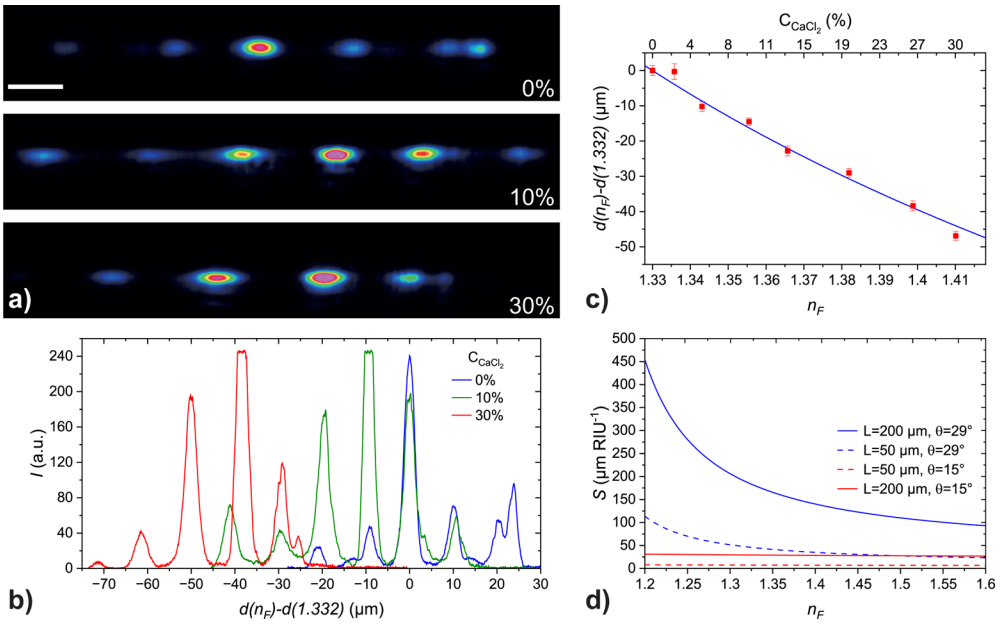

Fig. 5. (a) Measured near-field images for different C_CaCl_2 in a device configuration with $\theta = 29°$, $L = 200$, and an array with $d_{wg} = 10$ μm. (b) Corresponding profiles of the images in (a) shifted along the y-axis properly using the reference waveguide. The value of d for each solution is obtained as the centroid of the Gaussian function described by the intensities transmitted by the set of output waveguides. (c) d obtained by this analysis (red dots) versus the refractive index n_F of the solution, the blue line is Eq. (1). The errorbars correspond to the error obtained by the Gaussian fit on the centroids.

4.4. *Wavelength demultiplexing*

The shift d occurring to the light beam inside the channel depends also on the light wavelength λ by the $n_F(\lambda)$, as indicated in Eq. (1). A broadband light is, therefore, spectrally split across different output waveguides. When the output waveguide array collects different spectral components of the light, the system acts as a spectral demultiplexer. A graphical representation of the working principle of the demultiplexing operation is shown in Fig. 6(a). Due to dispersion inside the channel, the spectral components with longer wavelengths, such as red in the visible range, are refracted to a lower y coordinate (see Fig. 6(a)), than components with a shorter wavelength, such as green. The demultiplexing is evidenced in our system by scanning the output waveguides along y direction through a color CCD camera. The example in Fig. 6(b) shows the output of three consecutive waveguides with $d_{wg} = 25$ μm upon water injection in a 200 μm wide channel with the supercontinuum broadband source as input. There is a clear spectral difference between waveguides in Fig. 6(b), which reveals the occurrence of a demultiplexing process in the channel.

A quantitative spectral analysis has been performed by a spectral scan along the y-axis collecting a spectrum every 5 μm. The spectrum of each waveguide is considered as the local maxima of the transmitted power of this scan, as described in the procedure in section 7 of Supplement 1. An example of three spectra related to three consecutive waveguides is reported in Fig. 6(c), together with the transmitted spectrum of the reference waveguide and the source initial spectrum. The relative importance of the different components due to spectral dispersion inside the channel is clearly visible by comparing the three spectra with the reference and the source ones. Each spectrum has a range between 532 nm and 700 nm in agreement with the reference, but, for instance, longer wavelength components (red region) are enhanced at a lower y

Optics EXPRESS

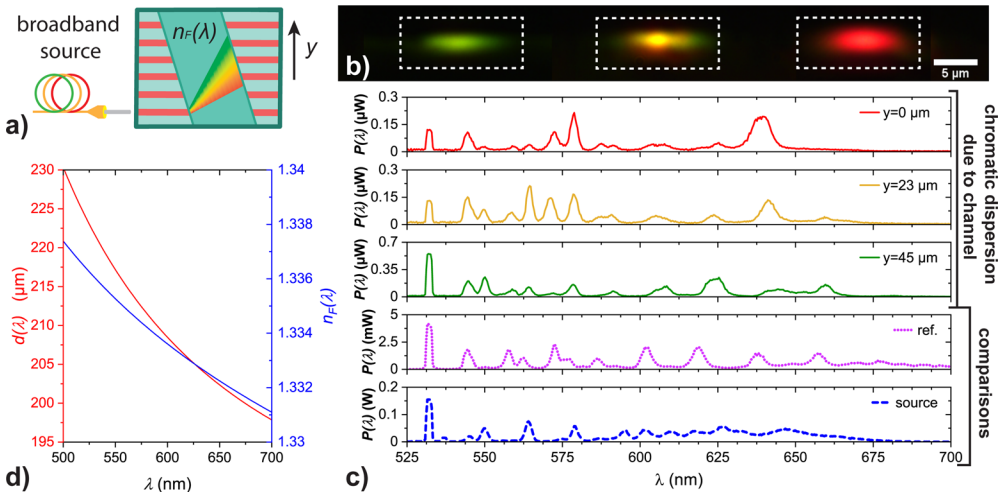

Fig. 6. (a) Sketch of the working principle and the y-scan measurement for the demultiplexing operation. (b) Outputs near-field CCD images from a d_{wg} = 25 µm array in a device with a L = 200 µm and θ = 30° channel with water. (c) Examples of spectra recorded during the scan along the y-axis, from the top to bottom: the spectrum recorded of the first waveguide (y=0 µm, red line), of the second one (y=23 µm, yellow line) and third one (45 µm, green line), of the reference waveguide (dotted pink line), and of the source (dashed blue line). (d) Calculated d versus wavelength (red curve) evaluated by Eq. (1) for L = 200 µm considering the dispersion relation of water $n_F(\lambda)$ plotted on the right axis in blue.

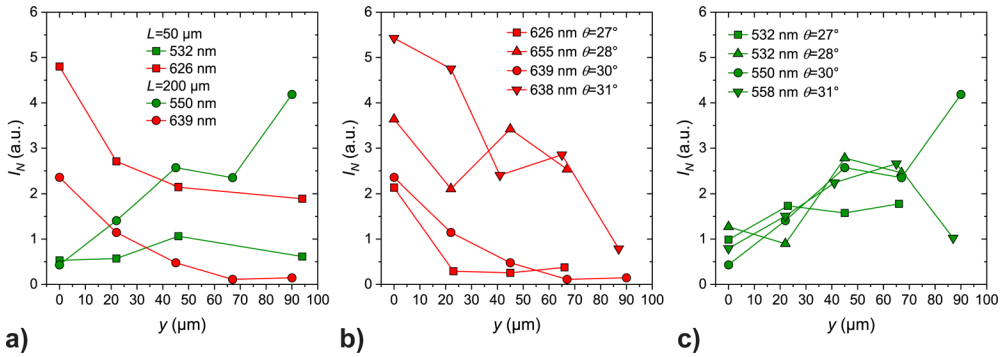

Fig. 7. (a) Spectral components against the position of the waveguides for two channels with the same θ = 30°. (b) Red components for a channel with L = 200 µm and different θ. The θ and exact wavelength are specified in the label. (c) is the corresponding graph to (b) but for green components.

coordinate. In agreement with Eq. (1), larger shifts d are observed for shorter wavelength and, conversely, for longer wavelength in the visible range as shown in red Fig. 6(d), according to the relation dispersion of water in blue in Fig. 6(d). Due to the low dispersion of water, wide angles are needed for the effective discrimination of spectral components. Larger dispersion can be achieved when the incidence angle is close to the critical angle and for more dispersive fluid. As a proof of concept, we used θ>25° and d_{wg} = 25 µm and water as fluid for the application herein presented and selected the two largest spectral components to analyze quantitatively the spectral separation capabilities. The choice of these parameters relies on the fact that a larger angle provides larger chromatic dispersion and large d_{wg} allows to collect the most dispersed

Optics EXPRESS

part of the spectra. For these two components, the integral I_N of the full peak at the selected wavelength (i.e., 4 nm intervals) is considered and normalized against the corresponding integral for the reference spectrum. The resulting values I_N are shown in Fig. 7(a) for two channels with different L. Figure 7(a) reveals that the I_N for red components are up to 5 times stronger in waveguides at smaller y coordinates, i.e., closer to the input waveguide and, therefore, at smaller d one, for both widths of the channel. Conversely, the green component is shifted towards the farther waveguides, from a negligible value of I_N in the first waveguide (at y=0 μm), up to about 4 times at the fifth waveguide (y=90 μm). For the wider channel, the spectral components reach a value close to zero with respect to the reference, thus achieving efficient spectral filtering. The demultiplexing can be further tuned with the tilt angle θ. Figure 7(b) and 7c report the I_N of red and green components, respectively, for channels with different θ. According to dispersion, channels with larger θ present a more pronounced spectral dispersion. The experimental data agree with this behavior, especially for the red components in Fig. 7(b), where I_N vary from 2 up to 5 times the reference increasing θ from 27° to 31°. For green components, the behavior is less evident due to the greater diffraction of the beam diameter across the channel, as described in detail in section 5 of Supplement 1.

5. Conclusion

An opto-microfluidic coupling between waveguide arrays and tilted fluidic channels in lithium niobate is presented in this work. In the proposed device, the channel with a tilted angle up to 30° has been considered and coupled with waveguides presenting optical quality interfaces. Light propagates through the interfaces between the channel and the waveguides by optical refraction. The optical path, therefore, depends on the optical properties of the fluid flowing in the channel. The system has proven to be an optimal playground for either optical or microfluidic applications, exploiting the flexible optical nature of the fluid or the probing properties of light.

The light beam inside the channel can couple into waveguides of the output array if the shift of the optical path matches the position of one of the output waveguides. We demonstrated that this coupling occurs and that the switch between two waveguides can be achieved upon the injection of the different media inside the channel. This feature enables also the optical sensing of the refractive index of the medium. Observing which waveguides in the array are transmitting light, the device acts as a digital, real-time optical probe of the refractive index of the fluid inside the channel. Finally, larger θ channels are demonstrated to be efficient wavelength demultiplexers, splitting different spectral components of the light due to the relation dispersion of the liquid inside the channel.

The system is used with different fluids, light sources of different wavelengths, and different coupling techniques. The LN is widely cited in optics, making easy a combination of this coupling with other optical methods. For example, the light transmission can be improved by pig-tailing stable bonded fiber, which is not suitable during the experimental phase but is optimal for stable and durable operation. Multiple waveguides could be coupled without effort in this way. In addition, the chemical resistance of the material and the robust monolithic structure of the device open up the possibility of using complex optical media such as light-diffusing media, colloidal suspension, and liquid crystal. For instance, 5CB liquid crystals have also a 2 times lower Abbe number than water and a well-known birefringence offering an interesting optical playground for light spectral manipulation operation.

It is also expected that the coupling herein proposed can be extended to other types of waveguides in LN [63], thus making the system very versatile. The material is very interesting in both the microfluidic and optical fields for its peculiar combination of properties, thus providing an additional tool to enhance the capabilities of optofluidics. We believe that the system can be scaled down to the nanofluidic size of the channel and one micrometer width waveguide, using other fabrication techniques, such as laser ablation [24]. It is also worth mentioning that

Optics EXPRESS

the integration into a single pocket-size substrate of both optical and microfluidic stages makes the device suitable for lab-on-a-chip applications. These features open various opportunities in different fields, such as point-of-care devices, medical diagnostic, or environmental sensing [64–66]. Furthermore, the close environment of the microfluidic channel combined with the strong chemical resistance of lithium niobate makes the system suitable for any chemical analysis. Although the initial cost is higher than traditional polymer-based devices, the robustness of the device combined with chemical resistance and real-time use makes it competitive with traditional disposable polymer devices and optimal for long-term use, such as environmental or medical monitoring.

Funding. Università degli Studi di Padova (BIRD165523/16); Université de Bourgogne (EUR-Eiphi ANR-17-EURE-0002).

Acknowledgments. This work has been supported by Projects No. BIRD165523/16 "Biosensing Light-driven Tools in Advanced Opto-microfluidic Lithium niobate Platform" and EUR-Eiphi N° ANR-17-EURE-0002. It was also partially supported by the French RENATECH network and its Femto-St technological facility. We acknowledge support from the open access publication fund of the University of Münster.

Disclosures. The authors declare no conflicts of interest.

Data availability. Data underlying the results presented in this paper are available in Dataset 1 [67].

Supplemental document. See Supplement 1 for supporting content.

References

1. B. E. Jones, "Optical fibre sensors and systems for industry," J. Phys. E: Sci. Instrum. **18**(9), 770–782 (1985).
2. D. Psaltis, S. R. Quake, and C. Yang, "Developing optofluidic technology through the fusion of microfluidics and optics," Nature **442**(7101), 381–386 (2006).
3. C. Monat, P. Domachuk, and B. Eggleton, "Integrated optofluidics: A new river of light," Nat. Photonics **1**(2), 106–114 (2007).
4. U. Levy and R. Shamai, "Tunable optofluidic devices," Microfluid. Nanofluid. **4**(1-2), 97–105 (2008).
5. X. Fan and S.-H. Yun, "The potential of optofluidic biolasers," Nat. Methods **11**(2), 141–147 (2014).
6. H. Schmidt and A. R. Hawkins, "The photonic integration of non-solid media using optofluidics," Nat. Photonics **5**(10), 598–604 (2011).
7. D. Erickson, D. Sinton, and D. Psaltis, "Optofluidics for energy applications," Nat. Photonics **5**(10), 583–590 (2011).
8. D. Brennan, J. Justice, B. Corbett, T. McCarthy, and P. Galvin, "Emerging optofluidic technologies for point-of-care genetic analysis systems: a review," Anal. Bioanal. Chem. **395**(3), 621–636 (2009).
9. X. Fan and I. M. White, "Optofluidic microsystems for chemical and biological analysis," Nat. Photonics **5**(10), 591–597 (2011).
10. N.-T. Huang, H.-l. Zhang, M.-T. Chung, J. H. Seo, and K. Kurabayashi, "Recent advancements in optofluidics-based single-cell analysis: optical on-chip cellular manipulation, treatment, and property detection," Lab Chip **14**(7), 1230–1245 (2014).
11. R. Blue and D. Uttamchandani, "Recent advances in optical fiber devices for microfluidics integration," J. Biophotonics **9**(1-2), 13–25 (2016).
12. L. Zhu, Y. Huang, and A. Yariv, "Integrated microfluidic variable optical attenuator," Opt. Express **13**(24), 9916–9921 (2005).
13. Y. Yang, A. Liu, L. Chin, X. Zhang, D. Tsai, C. Lin, C. Lu, G. Wang, and N. Zheludev, "Optofluidic waveguide as a transformation optics device for lightwave bending and manipulation," Nat. Commun. **3**(1), 651 (2012).
14. Y. Yang, L. Chin, J. Tsai, D. Tsai, N. Zheludev, and A. Liu, "Transformation optofluidics for large-angle light bending and tuning," Lab Chip **12**(19), 3785–3790 (2012).
15. N.-T. Nguyen, S. Lassemono, and F. A. Chollet, "Optical detection for droplet size control in microfluidic droplet-based analysis systems," Sens. Actuators, B **117**(2), 431–436 (2006).
16. Y. Zhao, X.-g. Hu, S. Hu, and Y. Peng, "Applications of fiber-optic biochemical sensor in microfluidic chips: A review," Biosens. Bioelectron. **166**, 112447 (2020).
17. P. Ashok, G. Singh, K. Tan, and K. Dholakia, "Fiber probe based microfluidic raman spectroscopy," Opt. Express **18**(8), 7642–7649 (2010).
18. V. Lien and F. Vollmer, "Microfluidic flow rate detection based on integrated optical fiber cantilever," Lab Chip **7**(10), 1352–1356 (2007).
19. F. Simoni, S. Bonfadini, P. Spegni, S. L. Turco, D. Lucchetta, and L. Criante, "Low threshold fabry-perot optofluidic resonator fabricated by femtosecond laser micromachining," Opt. Express **24**(15), 17416–17423 (2016).
20. R. M. Gerosa, A. Sudirman, L. d. S. Menezes, W. Margulis, and C. J. de Matos, "All-fiber high repetition rate microfluidic dye laser," Optica **2**(2), 186–193 (2015).

Optics EXPRESS

21. N. Bellini, F. Bragheri, I. Cristiani, J. Guck, R. Osellame, and G. Whyte, "Validation and perspectives of a femtosecond laser fabricated monolithic optical stretcher," Biomed. Opt. Express **3**(10), 2658–2668 (2012).
22. H. Wang, A. Enders, J.-A. Preuss, J. Bahnemann, A. Heisterkamp, and M. L. Torres-Mapa, "3d printed microfluidic lab-on-a-chip device for fiber-based dual beam optical manipulation," Sci. Rep. **11**, 1–12 (2021).
23. S. Liu, Z. Li, Z. Weng, Y. Li, L. Shui, Z. Jiao, Y. Chen, A. Luo, X. Xing, and S. He, "Miniaturized optical fiber tweezers for cell separation by optical force," Opt. Lett. **44**(7), 1868–1871 (2019).
24. R. Osellame, V. Maselli, R. M. Vazquez, R. Ramponi, and G. Cerullo, "Integration of optical waveguides and microfluidic channels both fabricated by femtosecond laser irradiation," Appl. Phys. Lett. **90**(23), 231118 (2007).
25. P. Friis, K. Hoppe, O. Leistiko, K. B. Mogensen, J. Hübner, and J. P. Kutter, "Monolithic integration of microfluidic channels and optical waveguides in silica on silicon," Appl. Opt. **40**(34), 6246–6251 (2001).
26. K. B. Mogensen, Y. C. Kwok, J. C. Eijkel, N. J. Petersen, A. Manz, and J. P. Kutter, "A microfluidic device with an integrated waveguide beam splitter for velocity measurements of flowing particles by fourier transformation," Anal. Chem. **75**(18), 4931–4936 (2003).
27. R. Zamboni, A. Zaltron, M. Chauvet, and C. Sada, "Real-time precise microfluidic droplets label-sequencing combined in a velocity detection sensor," Sci. Rep. **11**(1), 17987 (2021).
28. J. S. Kee, D. P. Poenar, P. Neuzil, and L. Yobas, "Monolithic integration of poly (dimethylsiloxane) waveguides and microfluidics for on-chip absorbance measurements," Sens. Actuators, B **134**(2), 532–538 (2008).
29. K. B. Mogensen, J. El-Ali, A. Wolff, and J. P. Kutter, "Integration of polymer waveguides for optical detection in microfabricated chemical analysis systems," Appl. Opt. **42**(19), 4072–4079 (2003).
30. M. Chauvet, L. Al Fares, B. Guichardaz, F. Devaux, and S. Ballandras, "Integrated optofluidic index sensor based on self-trapped beams in linbo3," Appl. Phys. Lett. **101**(18), 181104 (2012).
31. G. Bettella, R. Zamboni, G. Pozza, A. Zaltron, C. Montevecchi, M. Pierno, G. Mistura, C. Sada, L. Gauthier-Manuel, and M. Chauvet, "Linbo3 integrated system for opto-microfluidic sensing," Sens. Actuators, B **282**, 391–398 (2019).
32. L. Arizmendi, "Photonic applications of lithium niobate crystals," phys. stat. sol. (a) **201**(2), 253–283 (2004).
33. A. Boes, L. Chang, C. Langrock, M. Yu, M. Zhang, Q. Lin, M. Loncar, M. Fejer, J. Bowers, and A. Mitchell, "Lithium niobate photonics: Unlocking the electromagnetic spectrum," Science **379**(6627), eabj4396 (2023).
34. K. Buse, A. Adibi, and D. Psaltis, "Non-volatile holographic storage in doubly doped lithium niobate crystals," Nature **393**(6686), 665–668 (1998).
35. C. Wang, X. Xiong, N. Andrade, V. Venkataraman, X.-F. Ren, G.-C. Guo, and M. Lončar, "Second harmonic generation in nano-structured thin-film lithium niobate waveguides," Opt. Express **25**(6), 6963–6973 (2017).
36. F. Pettazzi, V. Coda, M. Chauvet, and E. Fazio, "Frequency-doubling in self-induced waveguides in lithium niobate," Opt. Commun. **272**(1), 238–241 (2007).
37. J. Lin, F. Bo, Y. Cheng, and J. Xu, "Advances in on-chip photonic devices based on lithium niobate on insulator," Photonics Res. **8**(12), 1910–1936 (2020).
38. D. Zhu, L. Shao, M. Yu, R. Cheng, B. Desiatov, C. Xin, Y. Hu, J. Holzgrafe, S. Ghosh, A. Shams-Ansari, E. Puma, N. Sinclair, C. Reimer, M. Zhang, and M. Loncar, "Integrated photonics on thin-film lithium niobate," Adv. Opt. Photonics **13**(2), 242–352 (2021).
39. M. Esseling, A. Zaltron, W. Horn, and C. Denz, "Optofluidic droplet router," Laser Photonics Rev. **9**(1), 98–104 (2015).
40. M. Wang, Z. Gao, X. Liu, L. Shi, Y. Mi, K. Gao, X. Zhang, and W. Yan, "Towards biochemical microreactor: Nonlocal photovoltaic actuation of aqueous microdroplets in oil-infused pdms channels based on linbo3: Fe crystal," Sens. Actuators, B **349**, 130819 (2021).
41. A. Puerto, S. Coppola, L. Miccio, V. Vespini, Á. García-Cabañes, M. Carrascosa, and P. Ferraro, "Droplet ejection and liquid jetting by visible laser irradiation in pyro-photovoltaic fe-doped linbo3 platforms," Adv. Mater. Interfaces **8**(22), 2101164 (2021).
42. A. Zaltron, D. Ferraro, A. Meggiolaro, S. Cremaschini, M. Carneri, E. Chiarello, P. Sartori, M. Pierno, C. Sada, and G. Mistura, "Optofluidic platform for the manipulation of water droplets on engineered linbo3 surfaces," Adv. Mater. Interfaces **9**(22), 2200345 (2022).
43. V. Marchesano, O. Gennari, L. Mecozzi, S. Grilli, and P. Ferraro, "Effects of lithium niobate polarization on cell adhesion and morphology," ACS Appl. Mater. Interfaces **7**(32), 18113–18119 (2015).
44. E. Muñoz-Cortés, A. Puerto, A. Blázquez-Castro, L. Arizmendi, J. L. Bella, C. López-Fernández, M. Carrascosa, and A. García-Caba nes, "Optoelectronic generation of bio-aqueous femto-droplets based on the bulk photovoltaic effect," Opt. Lett. **45**(5), 1164–1167 (2020).
45. A. Puerto, J. L. Bella, C. López-Fernández, A. García-Cabañes, and M. Carrascosa, "Optoelectronic manipulation of bio-droplets containing cells or macromolecules by active ferroelectric platforms," Biomed. Opt. Express **12**(10), 6601–6613 (2021).
46. J. Novotny, A. Lenshof, and T. Laurell, "Acoustofluidic platforms for particle manipulation," Electrophoresis **43**(7-8), 804–818 (2022).
47. M. Esseling, F. Holtmann, M. Woerdemann, and C. Denz, "Two-dimensional dielectrophoretic particle trapping in a hybrid crystal/pdms-system," Opt. Express **18**(16), 17404–17411 (2010).
48. S. Grilli, L. Miccio, V. Vespini, A. Finizio, S. De Nicola, and P. Ferraro, "Liquid micro-lens array activated by selective electrowetting on lithium niobate substrates," Opt. Express **16**(11), 8084–8093 (2008).

Optics EXPRESS

49. L. Miccio, A. Finizio, S. Grilli, V. Vespini, M. Paturzo, S. De Nicola, and P. Ferraro, "Tunable liquid microlens arrays in electrode-less configuration and their accurate characterization by interference microscopy," Opt. Express **17**(4), 2487–2499 (2009).
50. S. Bonfadini, F. Ciciulla, L. Criante, A. Zaltron, F. Simoni, V. Reshetnyak, and L. Lucchetti, "Optofluidic platform using liquid crystals in lithium niobate microchannel," Sci. Rep. **9**(1), 1062 (2019).
51. F. Ciciulla, A. Zaltron, R. Zamboni, C. Sada, F. Simoni, V. Y. Reshetnyak, and L. Lucchetti, "Optofluidic platform based on liquid crystals in x-cut lithium niobate: Thresholdless all-optical response," Crystals **11**(8), 908 (2021).
52. R. Barboza, S. Marni, F. Ciciulla, F. A. Mir, G. Nava, F. Caimi, A. Zaltron, N. A. Clark, T. Bellini, and L. Lucchetti, "Explosive electrostatic instability of ferroelectric liquid droplets on ferroelectric solid surfaces," Proc. Natl. Acad. Sci. **119**(32), e2207858119 (2022).
53. R. Zamboni, A. Zaltron, D. Ferraro, and C. Sada, "Droplet transition from non-axisymmetric to axisymmetric shape: Dynamic role of lubrication film in a rectangular microfluidic channel," Phys. Fluids **34**(12), 122014 (2022).
54. R. Zamboni, A. Zaltron, E. Izzo, G. Bottaro, D. Ferraro, and C. Sada, "Opto-microfluidic system for absorbance measurements in lithium niobate device applied to ph measurements," Sensors **20**(18), 5366 (2020).
55. L. Zanini, A. Zaltron, E. Turato, R. Zamboni, and C. Sada, "Opto-microfluidic integration of the bradford protein assay in lithium niobate lab-on-a-chip," Sensors **22**(3), 1144 (2022).
56. L. A. Fares, F. Devaux, B. Guichardaz, and M. Chauvet, "Self-trapped beams crossing tilted channels to induce guided polarization separators," Appl. Phys. Lett. **103**(4), 041111 (2013).
57. S. Fouchet, A. Carenco, C. Daguet, R. Guglielmi, and L. Riviere, "Wavelength dispersion of ti induced refractive index change in linbo 3 as a function of diffusion parameters," J. Lightwave Technol. **5**(5), 700–708 (1987).
58. G. Bettella, G. Pozza, S. Kroesen, R. Zamboni, E. Baggio, C. Montevecchi, A. Zaltron, L. Gauthier-Manuel, G. Mistura, C. Furlan, M. Chauvet, C. Denz, and C. Sada, "Lithium niobate micromachining for the fabrication of microfluidic droplet generators," Micromachines **8**(6), 185 (2017).
59. C.-Y. Tan and Y.-X. Huang, "Dependence of refractive index on concentration and temperature in electrolyte solution, polar solution, nonpolar solution, and protein solution," J. Chem. Eng. Data **60**(10), 2827–2833 (2015).
60. V. Pecheur, H. Porte, J. Hauden, F. Bassignot, M. Deroh, and M. Chauvet, "Watt-level shg in undoped high step-index ppln ridge waveguides," OSA Continuum **4**(5), 1404–1414 (2021).
61. H. Gong, A. T. Woolley, and G. P. Nordin, "High density 3d printed microfluidic valves, pumps, and multiplexers," Lab Chip **16**(13), 2450–2458 (2016).
62. J. T. Negou, L. A. Avila, X. Li, T. M. Hagos, and C. J. Easley, "Automated microfluidic droplet-based sample chopper for detection of small fluorescence differences using lock-in analysis," Anal. Chem. **89**(11), 6153–6159 (2017).
63. M. Bazzan and C. Sada, "Optical waveguides in lithium niobate: Recent developments and applications," Appl. Phys. Rev. **2**(4), 040603 (2015).
64. W. Jung, J. Han, J.-W. Choi, and C. H. Ahn, "Point-of-care testing (poct) diagnostic systems using microfluidic lab-on-a-chip technologies," Microelectron. Eng. **132**, 46–57 (2015).
65. P. Yager, T. Edwards, E. Fu, K. Helton, K. Nelson, M. R. Tam, and B. H. Weigl, "Microfluidic diagnostic technologies for global public health," Nature **442**(7101), 412–418 (2006).
66. R. Pol, F. Céspedes, D. Gabriel, and M. Baeza, "Microfluidic lab-on-a-chip platforms for environmental monitoring," TrAC, Trends Anal. Chem. **95**, 62–68 (2017).
67. R. Zamboni, "Data for "Opto-microfluidic coupling between optical waveguides and tilted microchannels in lithium niobate"," figshare (2023), https://doi.org/10.6084/m9.figshare.22819754.